Three-dimensional model for chemoresponsive polymer gels undergoing the Belousov-Zhabotinsky reaction

Olga Kuksenok,* Victor V. Yashin, and Anna C. Balazs
Chemical Engineering Department, University of Pittsburgh, Pittsburgh, Pennsylvania 15261, USA
(Received 23 June 2008; revised manuscript received 8 September 2008; published 22 October 2008)

We develop a computational model to capture the complex, three-dimensional behavior of chemoresponsive polymer gels undergoing the Belousov-Zhabotinsky reaction. The model combines components of the finite difference and finite element techniques and is an extension of the two-dimensional gel lattice spring model recently developed by two of us [V. V. Yashin and A. C. Balazs, J. Chem. Phys. **126**, 124707 (2007)]. Using this model, we undertake the first three-dimensional (3D) computational studies of the dynamical behavior of chemoresponsive BZ gels. For sufficiently large sample sizes and a finite range of reaction parameters, we observe regular and nonregular oscillations in both the size and shape of the sample that are coupled to the chemical oscillations. Additionally, we determine the critical values of these reaction parameters at the transition points between the different types of observed behavior. We also show that the dynamics of the chemoresponsive gels drastically depends on the boundary conditions at the surface of the sample. This 3D computational model could provide an effective tool for designing gel-based, responsive systems.

DOI: 10.1103/PhysRevE.78.041406 PACS number(s): 82.33.Ln, 82.40.Ck, 83.80.Kn

I. INTRODUCTION

Polymer gels constitute ideal candidates for creating active materials that can perform sustained mechanical work. This distinctive behavior is due to the fact that modulations in the surrounding solvent can drive a gel to undergo significant, rhythmic expansion and contraction [1,2]. The periodic modulations in the solvent can be introduced through chemistry; for example, there are a number of chemical reactions that lead to periodic variations in the pH of the solution [3,4]. When a pH-responsive gel is placed within this reactive bath, the polymer network exhibits pronounced oscillations in volume and shape. With these rhythmic oscillations, the chemical reaction in the solution is transduced into mechanical work. This form of work can be utilized to create pulsatile drug delivery devices [5] and potentially actuate artificial muscles [6].

By developing a more fundamental understanding of this form of chemomechanical transduction, we can better exploit the mechanism to design a variety of smart, responsive polymer networks. There have been a number of theoretical models for probing the behavior of oscillating gels [1,7–10]. These studies provided significant insight into the factors that contribute to the regular pulsations. The prior calculations, however, were carried out effectively in one dimension (1D) since the systems were assumed to be spherically symmetric. While these 1D calculations can describe the volumetric changes in the system, they cannot account for changes in the shape of the sample. Recently, two of us developed a two-dimensional model for oscillating gels [11,12]. This "gel lattice spring model" (gLSM) captures the shape changes and opens up the possibility of uncovering new morphological transitions within the gels.

In the previous studies [11,12], we specifically focused on a particular class of oscillating gels: those undergoing the Belousov-Zhabotinsky (BZ) reaction. Discovered in the 1950's, the BZ reaction is now recognized as a cornerstone of the field of nonlinear dynamical phenomena in chemically reacting systems [13]. The original reaction occurred in a fluid. Later, chemically neutral, nonresponsive polymer gels were used as a medium for BZ reactions in order to suppress hydrodynamic effects [14]. It was in the late 1990's when Yoshida fabricated the first chemoresponsive gel to undergo the BZ reaction [15]. The BZ gels are unique because the polymer network can expand and contract periodically without external stimuli [15–20]. This autonomous, self-oscillatory behavior is due to a ruthenium catalyst, which is covalently bonded to the polymers. The BZ reaction generates a periodic oxidation and reduction of the anchored metal ion, which changes the hydrophilicity of the polymer chains, and in this way, the chemical oscillations induce the rhythmic swelling and deswelling in the gel [15–20]. Via our 2D gLSM approach, we were able to uncover [11,12] a rich variety of spatiotemporal patterns and shape changes that occurred due to the coupling between chemistry and mechanics in these BZ gels.

In another study using the 2D gLSM [21], we demonstrated how an applied mechanical compression could be harnessed to drive an initially nonoscillating BZ gel into the oscillatory regime, or drive the system from one oscillatory pattern to another. We isolated a scenario where the application of the force caused the material to undergo spontaneous and autonomous rotation of the entire sample. We also showed that by initiating a unidirectional, propagating chemical wave, we could drive the entire gel sample to move in the opposite direction [12].

The results of the above 2D simulations pointed to the possibility that BZ gels could act as a sensing system, which responds to a local impact by sending a signal (a chemical wave) throughout the entire sample. In the 2D model, however, the swelling of the gel in the third (vertical) direction was constrained to a constant value, so we could only model the effects of a spatially uniform deformation (e.g., uniform

*olk2@pitt.edu

compression). To probe the effects of a spatially localized impact, it was necessary to develop a 3D model, which allows for local variations in the degree of vertical swelling. Moreover, just as the 2D model of chemoresponsive BZ gels enabled us to study pattern formation and shape changes that were not possible in 1D [11,12], the 3D model could reveal even richer dynamics of this nonlinear system and unique three-dimensional shape changes. There are indeed a number of examples where the nonlinear chemical dynamics in a deformable medium give rise to unique 3D morphological changes of this medium. For example, chemomechanical instabilities in responsive gels were experimentally demonstrated to cause propagating, traveling waves of changes in volume [22]. As another example, it was recently shown that the main features of pattern and shape selection in plants could be viewed as resulting from a coupling of oscillating chemical dynamics to the three-dimensional surface growth [23]. In the latter work [23], researchers utilized a finite element technique to develop a three-dimensional model that couples chemical oscillations to a shape selection during the plant growth.

In the current paper, we extend the 2D gLSM for BZ gels to three dimensions, allowing us to undertake computational studies to probe the dynamical behavior of the responsive BZ gels in 3D and thereby obtain a more complete understanding of the interplay between the finite deformations of a responsive medium and nonlinear chemical dynamics. The computational efficiency of the model enables us to simulate the dynamics of relatively large samples in realistic time frames. Herein, we determine the effect of the sample size and the reaction parameters on the behavior of the system. We also examine how the boundary conditions at the surface of the sample affect the pattern formation.

In the following section, we first describe the system of equations that governs the dynamics of responsive BZ gels (see Sec. II A). In Sec. II B, we describe how we formulated the 3D gLSM to solve these continuum equations. Readers who are more interested in the results than the details of the methodology can go directly to Sec. II C, where we describe how we validated this approach. In this subsection, we also focus on one of the limiting cases that can be solved via an independent method and compare the latter results with the findings from the gLSM. Using the validated approach, we then carried out the studies described in Sec. III. In Sec. IV, we outline studies that are made possible with this approach.

II. MODEL

A. Governing continuum equations

An experimental example of a BZ gel is the cross-linked polymer network of poly(N-isopropylacrylamide) (NIPAAm) in which the catalyst ruthenium tris(2,2′-bipyridine) [$Ru(bpy)_3$] is anchored onto the polymer chains [15–20]. This polymer network is swollen in an aqueous solution of $NaBrO_3$, HNO_3, and malonic acid (MA). While the kinetics of the BZ reaction involves two dozen variables for the concentrations of reactive species, as well as tens of chemical reactions, it is often successfully described in terms of Field-Koros-Noyes (FKN) mechanism [24], which can be reduced to only three basic processes. The "Oregonator" model is widely used to describe the FKN mechanism [24,25]. The Tyson and Fife formulation of the Oregonator model [25] was recently modified [10] to account explicitly for the effect of the polymer network on the BZ reaction.

Using this modified Oregonator model [10], the dynamics of chemoresponsive gels undergoing the BZ reaction can be described in terms of the volume fraction of polymer ϕ and the dimensionless concentrations of the dissolved intermediate u and the oxidized metal-ion catalyst v. The dimensionless variables u and v are defined using the parametrization by Tyson and Fife [25]. We also note that these concentrations are defined with respect to the total volume of the system [10–12]. The dynamic behavior of this system is governed by the following dimensionless equations (details concerning the derivation of these equations can be found in Ref. [12]):

$$\frac{d\phi}{dt} = -\phi \nabla \cdot \mathbf{v}^{(p)}, \tag{1}$$

$$\frac{dv}{dt} = -v \nabla \cdot \mathbf{v}^{(p)} + \varepsilon G(u,v,\phi), \tag{2}$$

$$\frac{du}{dt} = -u \nabla \cdot \mathbf{v}^{(p)} + \nabla \cdot \left[\mathbf{v}^{(p)} \frac{u}{1-\phi} \right] + \nabla \cdot \left[(1-\phi) \nabla \frac{u}{1-\phi} \right] + F(u,v,\phi). \tag{3}$$

Here $\frac{d}{dt} \equiv \frac{\partial}{\partial t} + \mathbf{v}^{(p)} \cdot \nabla$ denotes the material time derivative associated with the polymer velocity $\mathbf{v}^{(p)}$, which is defined in the laboratory coordinate system. We assume that it is solely the polymer-solvent interdiffusion that contributes to the gel dynamics and neglect the total velocity of the polymer-solvent system [12]. Hence, in Eq. (3), we took into account that

$$\phi \mathbf{v}^{(p)} + (1-\phi)\mathbf{v}^{(s)} \equiv 0, \tag{4}$$

where $\mathbf{v}^{(s)}$ is the velocity of the solvent. The third term on the right hand side (RHS) of Eq. (3) describes the contribution from the diffusion flux of the dissolved reagent u [12]. The functions $G(u,v,\phi)$ and $F(u,v,\phi)$ in Eqs. (2) and (3) describe the kinetics of the BZ reaction and are based on the Oregonator model for BZ reactions in solution [25]. These terms have been modified to explicitly account for the effect of the polymer on the BZ reaction, namely [10],

$$F(u,v,\phi) = (1-\phi)^2 u - u^2 - (1-\phi) f v \frac{u - q(1-\phi)^2}{u + q(1-\phi)^2}, \tag{5}$$

$$G(u,v,\phi) = (1-\phi)^2 u - (1-\phi) v. \tag{6}$$

We note that the stoichiometric factor f and the dimensionless parameters ε and q have the same meaning as in the original Oregonator model [24,25]. The stoichiometric parameter f effectively specifies the concentration of oxidized catalyst ν within the system in the steady state and affects the amplitude of the oscillations in the oscillatory state [24]. The dynamics of the polymer network is assumed to be purely relaxational [26], so that the forces acting on the deformed

gel are balanced by the frictional drag due to the motion of the solvent. Thus, we can write [12]

$$\nabla \cdot \hat{\boldsymbol{\sigma}} = \Lambda_0^{-1}(\phi/\phi_0)^{3/2}(\mathbf{v}^{(p)} - \mathbf{v}^{(s)}), \tag{7}$$

where $\hat{\boldsymbol{\sigma}}$ is the dimensionless stress tensor measured in units $v_0^{-1}T$, where v_0 is the volume of a monomeric unit, T is temperature measured in energy units, and ϕ_0 is the volume fraction of the polymer in the undeformed state. The mobility of the polymer gel in Eq. (7) is characterized by the dimensionless kinetic coefficient $\Lambda_0 = T[v_0\zeta(\phi_0)D_u]^{-1}$, where D_u is the diffusion coefficient and $\zeta(\phi)$ is the polymer-solvent friction coefficient. Following Ref. [26], in Eq. (7) we took into account that $\zeta(\phi) = \zeta(\phi_0)(\phi/\phi_0)^{3/2}$; this approximation for the friction coefficient is valid in the semidilute and intermediate regimes (i.e., for $\phi < 0.5$, which is always the case in the following calculations).

If the stress tensor $\hat{\boldsymbol{\sigma}}$ is known, the polymer and solvent velocities can be calculated from Eqs. (4) and (7). The stress tensor can be derived from the energy density of the deformed gel U, which consists of the elastic energy density associated with the deformations U_{el} and the polymer-solvent interaction energy density U_{FH}. Thus, we can write $U = U_{\mathrm{el}}(I_1, I_3) + U_{\mathrm{FH}}(I_3)$, where $I_1 = \mathrm{tr}\hat{\mathbf{B}}$ and $I_3 = \det \hat{\mathbf{B}}$ are the invariants of the left Cauchy-Green strain tensor $\hat{\mathbf{B}} = \hat{\mathbf{F}} \cdot \hat{\mathbf{F}}^T$, $\hat{\mathbf{F}}$ is the deformation-gradient tensor [27], and the superscript "T" stands for the transposition operator. The third invariant I_3 is related to the volume change during the deformation as $I_3^{1/2} = dV/dV_0$ [27], where dV_0 and dV denote the volumes in the undeformed and deformed states, respectively.

The elastic energy U_{el} describes the rubber elasticity of the crosslinked polymer chains and is proportional to the crosslink density c_0 (the number density of elastic strands in the undeformed polymer network). This term can be written as

$$U_{\mathrm{el}} = \frac{c_0 v_0}{2}(I_1 - 3 - \ln I_3^{1/2}). \tag{8}$$

The energy of the interaction between the polymer and solvent can be written in the Flory-Huggins form as

$$U_{\mathrm{FH}} = \sqrt{I_3}[(1-\phi)\ln(1-\phi) + \chi_{\mathrm{FH}}(\phi)\phi(1-\phi) - \chi^* v(1-\phi)]. \tag{9}$$

The factor $\sqrt{I_3}$ appears in Eq. (9) because the energy density is defined with respect to a unit volume in the undeformed state. Specifically, the local volume fraction of the polymer in the deformed gel depends on the volume fraction of the polymer in the undeformed state ϕ_0 as $\phi = \phi_0 I_3^{-1/2}$. The $\chi_{\mathrm{FH}}(\phi)$ is the polymer-solvent interaction parameter and χ^* is an adjustable parameter in the model. With $\chi^* > 0$, the last term on the RHS of Eq. (9) describes the hydrating effect of the oxidized metal-ion catalyst on the polymer chains [10]. This hydrating effect (observed experimentally in Refs. [15–20]) arises from the inclusion of the $\mathrm{Ru}(bpy)_3$ complex, which changes the phase transition temperature and the maximum degree of swelling to an extent that depends on the electric charge of the metal ion [15–17]. By varying the oxidation state of $\mathrm{Ru}(bpy)_3$, it has been shown experimentally that the oxidation of $\mathrm{Ru}(bpy)_3$ results in an increase in the degree of gel swelling [15–20]. In effect, the last term in Eq. (9) defines the coupling between the chemical and mechanical degrees of freedom in the system. Using Eqs. (8) and (9), one can derive the following constitutive equation for the swollen, chemoresponsive polymer gel [12]:

$$\hat{\sigma} = -P(\phi, v)\hat{\mathbf{I}} + c_0 v_0 \frac{\phi}{\phi_0}\hat{\mathbf{B}}. \tag{10}$$

Here, $\hat{\mathbf{I}}$ is the unit tensor and the pressure $P(\phi, v)$ is defined as [12]

$$P(\phi, v) = \pi_{\mathrm{osm}}(\phi, v) + c_0 v_0 \phi/2\phi_0, \tag{11}$$

with the contribution from the osmotic pressure of the polymer being $\pi_{\mathrm{osm}}(\phi, v) = I_3^{-1/2}(-U_{\mathrm{FH}} + \phi\partial U_{\mathrm{FH}}/\partial\phi + v\partial U_{\mathrm{FH}}/\partial v)$, which can be written as [12]

$$\pi_{\mathrm{osm}} = -[\phi + \ln(1-\phi) + \chi(\phi)\phi^2] + \chi^* v\phi, \tag{12}$$

where $\chi(\phi) = \chi_0 + \chi_1\phi$, according to the expression given in Ref. [28]. We note that $\chi(\phi) = \chi_{\mathrm{FH}}(\phi) - (1-\phi)\partial\chi_{\mathrm{FH}}(\phi)/\partial\phi$; it coincides with the Flory-Huggins interaction parameter in Eq. (9) only when there is no dependence on the polymer volume fraction, i.e., when $\chi_{\mathrm{FH}} = \chi_0$.

The gel can attain a steady state if the elastic stresses are balanced by the osmotic pressure and, simultaneously, the reaction exhibits a stationary regime for the same system parameters. More specifically, such stationary solutions $(\phi_{\mathrm{st}}, u_{\mathrm{st}}, v_{\mathrm{st}})$ can be found by numerically solving the following system of equations:

$$c_0 v_0\left[\left(\frac{\phi_{\mathrm{st}}}{\phi_0}\right)^{1/3} - \frac{\phi_{\mathrm{st}}}{2\phi_0}\right] = \pi_{\mathrm{osm}}(\phi_{\mathrm{st}}, v_{\mathrm{st}});$$

$$F(u_{\mathrm{st}}, v_{\mathrm{st}}, \phi_{\mathrm{st}}) = 0; \quad G(u_{\mathrm{st}}, v_{\mathrm{st}}, \phi_{\mathrm{st}}) = 0. \tag{13}$$

The left-hand side of the first equation in Eq. (13) represents an elastic stress, as shown in Ref. [12]. If the solution of the system of equations in Eq. (13) is known, the corresponding stationary degree of swelling can be calculated as $\lambda_{\mathrm{st}} = (\phi_0/\phi_{\mathrm{st}})^{1/3}$. It is worth noting that Eq. (13) describes a gel that swells with no restrictions in all three dimensions.

To simulate the dynamical behavior of this system, we develop a three-dimensional gel lattice spring model (gLSM) described in detail below. This approach is an extension of the 2D gLSM computational technique recently developed by two of us [11,12]. As discussed below, we tested the model and confirmed that the simulations are robust and that the model could readily be used for a wide range of parameters. For a set of reference parameters, we chose values from the available experimental data. In particular, for the BZ reaction parameters, we set $\varepsilon = 0.354$ and $q = 9.52 \times 10^{-5}$ (based on the experimental data provided in Ref. [16] and in Ref. [29]) and for the parameters characterizing the properties of the gel, we set $\phi_0 = 0.139$, and $c_0 = 1.3 \times 10^{-3}$ (based on the experimental data provided in Ref. [30]), and $\Lambda_0 = 100$ (this value is chosen to be the same as in Ref. [12]). The details of the derivation of these parameters, as well as actual experimental data used in these derivations, are provided in Tables I and II of Ref. [12]. For the interaction

parameters in Eq. (12), we use $\chi_0=0.338$ and $\chi_1=0.518$. To calculate these values, we use the temperature dependence of χ_0 for nonresponsive polymer gels given by Hirotsu in Ref. [28], and calculate this value at 20 °C for a gel with the above values of ϕ_0 and c_0. We also set $\chi^*=0.105$; χ^* is an adjustable parameter of the model and is chosen to have the same value as in Refs. [11,12]. For these parameters, the dimensionless units of time and length in our simulations correspond to ~1 s and ~40 μm, respectively (the estimates are provided in Refs. [11,12]).

B. Formulation of the gLSM model in three dimensions

We represent a 3D element of the reactive gel by a general linear hexahedral element with the node numbering shown in Fig. 1 [31–33]. The whole gel sample consists of $(L_x-1)\times(L_y-1)\times(L_z-1)$ elements; here L_i is the number of nodes in the i direction, $i=x,y,z$. Within each element $\mathbf{m}\equiv(i,j,k)$, the concentrations of the dissolved reagent $u(\mathbf{m})$, the oxidized metal-ion catalyst $v(\mathbf{m})$, and the volume fraction of polymer $\phi(\mathbf{m})$ are taken to be spatially uniform. The total energy of the deformed sample U_{tot} can be calculated by summing over the energies of all the deformed elements; that is, $U_{\text{tot}}=\Delta^3\Sigma_{\mathbf{m}}U(\mathbf{m})$, where $U(\mathbf{m})$ is the energy density of the deformed element $\mathbf{m}$ defined with respect to its volume in the undeformed state, and Δ is the linear size of the undistorted element. From these energy densities, we can calculate the forces acting on the nodes of the element. To carry out the latter calculation and integrate the evolution equation for v and u [see Eqs. (2) and (3)], we first define a coordinate system (ξ,η,ζ) local to this element (as marked in Fig. 1) and perform all the relevant integrations in this local coordinate system, as detailed in Sec. 1 of the Appendix.

If the coordinates of all the nodes of a given element are known, we can calculate the volume of this element [see Eq. (A3) of Sec. 1 of the Appendix] and consequently, determine the volume fraction of polymer within this element as

$$\phi(\mathbf{m})=\frac{\Delta^3\phi_0}{V(\mathbf{m})}, \tag{14}$$

where Δ is the linear size of the element in the undistorted state. If the values of $\phi(\mathbf{m})$ and $v(\mathbf{m})$ are known within each element $\mathbf{m}$, we can calculate the forces acting on each node from all the neighboring elements and the velocities of all the nodes (see below). We can then numerically calculate the new positions of the nodes and the updated values of u and v according to the evolution equations (2) and (3), in which the value of ϕ is expressed through Eq. (14). In what follows, we describe each of these steps.

The total force acting on each node contains contributions from the elastic and osmotic properties of the system. Namely, it was shown [12] that the total force acting on the node n of the element $\mathbf{m}$ consists of two contributions: the first, $\mathbf{F}_{1,n}(\mathbf{m})$, originates from the first term on the RHS of Eq. (8) for the elastic energy, and the second, $\mathbf{F}_{2,n}(\mathbf{m})$, accounts for the isotropic pressure within this element, as defined in Eq. (11).

The first contribution to the total force acting on the node n of the element $\mathbf{m}$, the springlike force $\mathbf{F}_{1,n}(\mathbf{m})$, can be calculated from $\mathbf{F}_{1,n}(\mathbf{m})=-\partial U_1/\partial\mathbf{r}_n(\mathbf{m})$, where $U_1=\Delta^3\Sigma_{\mathbf{m}}U_1(\mathbf{m})$ and the summation is made over all the elements in the sample. The details of the calculation of $U_1(\mathbf{m})$ are provided in Sec. 2 of the Appendix. It can be shown that this force has the following form:

$$\mathbf{F}_{1,n}(\mathbf{m})=\frac{c_0v_0\Delta}{12}\left(\sum_{NN(\mathbf{m}')}w(n',n)[\mathbf{r}_{n'}(\mathbf{m}')-\mathbf{r}_n(\mathbf{m})]+\sum_{NNN(\mathbf{m}')}[\mathbf{r}_{n'}(\mathbf{m}')-\mathbf{r}_n(\mathbf{m})]\right). \tag{15}$$

Here, $\Sigma_{NN(\mathbf{m}')}$ and $\Sigma_{NNN(\mathbf{m}')}$ represent the respective summations over all the next-nearest neighbor nodal pairs and next-next-nearest neighbor nodal pairs belonging to all the neigh-

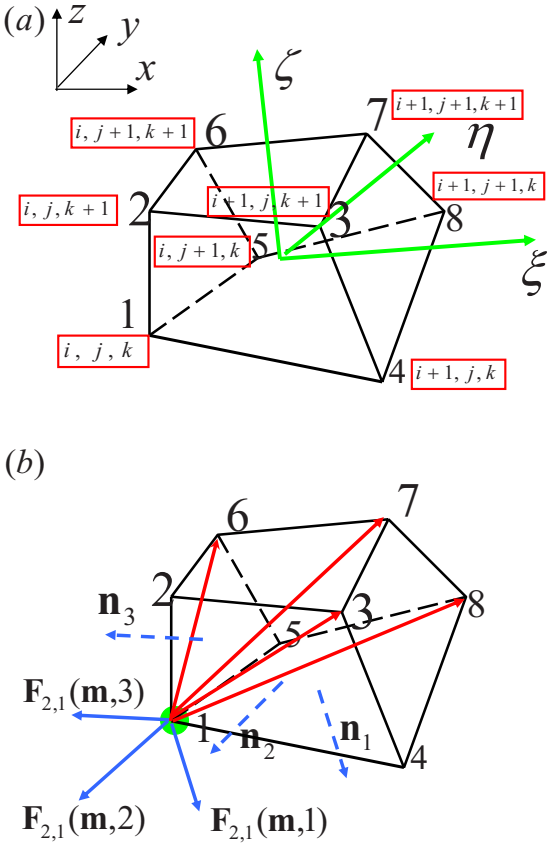

FIG. 1. (Color online) Schematic of the 3D element. (a) For each node, we provide its numbering within the element (1-8) and its numbering with respect to the entire sample [see frames (red online) next to each node]. The entire sample consists of $L_x\times L_y\times L_z$ nodes. In the underfomed state, the set of indexes $i=1\cdots L_x$, $j=1\cdots L_y$, and $k=1\cdots L_z$ defines the position of the nodes in x, y, and z directions, correspondingly. Coordinate system local to this element (ξ,η,ζ) is marked by gray (green online) arrows. (b) Forces acting on the node 1 [marked by the gray (green online) circle] of the element $\mathbf{m}=(i,j,k)$. The gray arrows (red online) inside the element mark the spring-like elastic forces acting between the node 1 and the next-nearest and next-next-nearest neighbors within the same element $\mathbf{m}$ [as defined in Eq. (21)]. The gray arrows (blue online) outside of the element mark contributions to nodal forces from the isotropic pressure within this element [as defined in Eq. (22)].

boring elements $\mathbf{m}'$ adjacent to the node n of the element $\mathbf{m}$. We note that if the next-nearest nodes n and n' belong to an internal face (i.e., a face that belongs to two neighboring elements), the springlike force between these nodes should be accounted for twice in Eq. (15) due to the contributions from the two adjacent elements. Hence, $w(n',n)=2$ in Eq. (15) if n and n' belong to an internal face and $w(n',n)=1$ in Eq. (15) if n and n' belong to a boundary face. We note that unlike the case of purely two-dimensional deformations [12], there is no contribution from the interaction between the nearest-neighbor nodes in Eq. (15).

The second contribution to the total force acting on the node n of the element $\mathbf{m}$, $\mathbf{F}_{2,n}(\mathbf{m})$, accounts for the isotropic pressure within this element, as defined in Eq. (11) (the derivation is provided in Ref. [12]). In other words, $\mathbf{F}_{2,n}(\mathbf{m})$ includes both the contribution from the osmotic pressure due to the polymer-solvent interactions (involving χ_{FH} and χ^*) and the contribution from the elastic energy that was not accounted for in the calculation of the springlike elastic forces [Eq. (15)]. For a three-dimensional element, this force can be written in the following form:

$$\mathbf{F}_{2,n}(\mathbf{m}) = \frac{1}{4}\sum_{\mathbf{m}'} P[\phi(\mathbf{m}'),v(\mathbf{m}')][\mathbf{n}_1(\mathbf{m}')S_1(\mathbf{m}') + \mathbf{n}_2(\mathbf{m}')S_2(\mathbf{m}') + \mathbf{n}_3(\mathbf{m}')S_3(\mathbf{m}')]. \quad (16)$$

In the above equation, the summation is performed over all the neighboring elements $\mathbf{m}'$ that include the node n of the element $\mathbf{m}$. The pressure within each element, $P[\phi(\mathbf{m}'),v(\mathbf{m}')]$ is calculated according to Eq. (11). In Eq. (16), the vector $\mathbf{n}_{i(\mathrm{face})}(\mathbf{m}')$ is the outward normal to the face i(face) of the element $\mathbf{m}'$, and $S_{i(\mathrm{face})}$ is the area of this face (for more details, see Sec. 1 of Appendix). For illustration, the vectors $\mathbf{n}_{i(\mathrm{face})}(\mathbf{m})$ are shown in Fig. 1(b) for the chosen element $\mathbf{m}' \equiv \mathbf{m}$ that includes the node $n=1$ [marked by the gray (green online) circle]. In this figure, the faces i(face) $=1$, i(face)$=2$, and i(face)$=3$ correspond to the $\zeta=-1$, $\eta=-1$, and $\xi=-1$ in the local coordinate system, respectively.

Both contributions to the nodal force acting on the node $n=1$ of the element $\mathbf{m}$ from within this element are shown schematically in Fig. 1(b). The contributions from the springlike forces from the interaction between the node $n=1$ and the next-nearest and next-next-nearest nodes within the element $\mathbf{m}$ are marked by red arrows. The contributions from the forces $\mathbf{F}_{2,n}(\mathbf{m})$ are depicted by the corresponding gray arrows (blue online), with the contribution from i(face) marked by $\mathbf{F}_{2,n}[\mathbf{m},i(\mathrm{face})]$ [here, $i(\mathrm{face})=1,2,3$]. It is important to emphasize that the total force acting on the node n of the element $\mathbf{m}$ includes similar contributions from each of the neighboring elements containing this node if this node is an internal node (and, correspondingly, if the node 1 is a corner node, it includes only the contributions to the total force listed above and depicted in the Fig. 1).

If the forces acting on the node n of the element $\mathbf{m}$ are known, we can calculate its velocity in the overdamped regime as [11,12]

$$\frac{d\mathbf{r}_n(\mathbf{m})}{dt} = M_n(\mathbf{m})[F_{1,n}(\mathbf{m}) + F_{2,n}(\mathbf{m})], \quad (17)$$

here $M_n(\mathbf{m})$ is the mobility of the node. We calculate the mobility $M_n(\mathbf{m})$ in the same manner as was done for the case of purely 2D deformations in Ref. [12]; here, however, we make the appropriate corrections for our 3D system. Namely, we integrate Eq. (7) over the volume of the element $\mathbf{m}$, and estimate the integral on the right hand side of this equation by evaluating the values of the integrand on all the nodes of the element $\mathbf{m}$. This allows us to calculate the nodal friction coefficients and consequently, to estimate the mobility of the node n of the element $\mathbf{m}$ in the following form:

$$M_n(\mathbf{m}) = 8\frac{\Lambda_0\sqrt{\phi_0}}{\Delta^3}\frac{(1-\langle\phi(\mathbf{m})\rangle_n)}{\sqrt{\langle\phi(\mathbf{m})\rangle_n}}. \quad (18)$$

In the above equation, $\langle\phi(\mathbf{m})\rangle_n$ denotes the approximate value of the polymer volume fraction at the node n of the element $\mathbf{m}$; to calculate this value, we take an average value of the $\phi(\mathbf{m}')$ over all the elements $\mathbf{m}'$ adjacent to the node n of the element $\mathbf{m}$, i.e., for the internal node, $\langle\phi(\mathbf{m})\rangle_n = \frac{1}{8}\Sigma_{\mathbf{m}'}\phi(\mathbf{m}')$.

All the above expressions allow us to formulate the discretized evolution equations for our model. By calculating the nodal displacements as defined in Eq. (17), we effectively integrate the first equation of our governing system of equations (1)–(3) defined above. More specifically, at each simulation time step Δt, we update the positions of all the nodes as

$$\mathbf{r}_n(\mathbf{m},t+\Delta t) = \mathbf{r}_n(\mathbf{m}) + \Delta t M_n(\mathbf{m})[F_{1,n}(\mathbf{m}) + F_{2,n}(\mathbf{m})], \quad (19)$$

where $M_n(\mathbf{m})$, $\mathbf{F}_{1,n}(\mathbf{m})$, and $\mathbf{F}_{2,n}(\mathbf{m})$ are calculated using Eqs. (18), (15), and (16), respectively. We then update the value of the volume fraction of the polymer using Eq. (14). In Eq. (19), $\mathbf{r}_n(\mathbf{m},t+\Delta t)$ and $\mathbf{r}_n(\mathbf{m})$ represent the coordinates of the node n of the element $\mathbf{m}$ at simulation times $t+\Delta t$ and t, respectively.

To simulate the dynamics of the whole system, we also need to numerically integrate Eqs. (2) and (3). Below, we provide the discretized evolution equations that we use to update the concentrations of the dissolved reagent and the oxidized metal-ion catalyst in our sample during the time step Δt; in these equations, $u(\mathbf{m},t+\Delta t)$, $v(\mathbf{m},t+\Delta t)$, $\phi(\mathbf{m},t+\Delta t)$ and $u(\mathbf{m})$, $v(\mathbf{m})$, $\phi(\mathbf{m})$ represent the values of the variables within the element $\mathbf{m}$ at the simulation times $t+\Delta t$ and t, respectively.

Using Eqs. (2) and (3), we can write the following:

$$v(\mathbf{m},t+\Delta t) = v(\mathbf{m}) + \Delta t\{-v(\mathbf{m})T_0(\mathbf{m}) + \varepsilon G[u(\mathbf{m}),v(\mathbf{m}),\phi(\mathbf{m})]\}, \quad (20)$$

$$u(\mathbf{m},t+\Delta t) = u(\mathbf{m}) + \Delta t\{-u(\mathbf{m})T_0(\mathbf{m}) + T_1(\mathbf{m}) + T_2(\mathbf{m}) + F[u(\mathbf{m}),v(\mathbf{m}),\phi(\mathbf{m})]\}, \quad (21)$$

where the terms $T_0(\mathbf{m})$, $T_1(\mathbf{m})$, and $T_2(\mathbf{m})$ are defined in detail in Sec. 3 of the Appendix below.

To implement different types of boundary conditions for the concentration $\mathbf{u}$, we define certain "service elements;" a single layer of these service elements is located outside each of the faces of the gel sample. For the case of the no-flux boundary conditions, we update the values of $\tilde{u}$, the normalized concentration of the dissolved reagent $\{\tilde{u}(\mathbf{m})=u(\mathbf{m})[1$

$-\phi(\mathbf{m})]^{-1}\}$, and ϕ within these service elements at each time step in such a way that we ensure zero flux of the dissolved reagent through the surface of the sample (i.e., we set these values equal to the corresponding values of $\tilde{u}$ and ϕ in the neighboring boundary element within the sample). Alternatively, if we want to account for a flux of the reactant u through the surface of the sample, but assume that its value is kept fixed outside the sample, we correspondingly keep the value of u fixed at a chosen value within all the service elements. (For example, $u=0$ in one of the simulation runs below.) For simplicity, we assume that the distance between the centers of the service element and the boundary element is the same as the distance between the centers of this boundary element and the neighboring internal element within the sample. We note that in most of the simulations described below, we use the no-flux boundary conditions.

Finally, we comment on the choice of the simulation time step Δt in Eqs. (19)–(21). It is known that the BZ reaction equations are stiff and, correspondingly, a sufficiently small time step is required to update the values of u and v as the reaction takes place. On the other hand, our simulations indicated that the terms $T_1(\mathbf{m})$ and $T_2(\mathbf{m})$ in Eqs. (21), the positions of all the nodes [Eq. (19)], and, correspondingly, the term $T_0(\mathbf{m})$ [see Eq. (A8)], can be updated with a larger time step. Correspondingly, we use two simulation time steps: the larger value Δt_X is a time step we use to update the positions of the nodes [Eq. (19)], the volume fractions of the polymer [Eq. (14)] and the terms $T_0(\mathbf{m})$, $T_1(\mathbf{m})$, and $T_2(\mathbf{m})$ [Eqs. (A8), (A9), and (A11), respectively]; we use the smaller value Δt to update the values of u and v according to Eqs. (20) and (21). [Here, we update reaction terms at each time step $t+\Delta t$, while we use the values of $T_0(\mathbf{m})$, $T_1(\mathbf{m})$, and $T_2(\mathbf{m})$ updated with the time step Δt_X.] The use of two time steps allows us to speed up the simulation without loosing accuracy; the criteria we use to select an appropriate factor $\Delta t_X/\Delta t$ is that the difference between the simulation results obtained with the chosen $\Delta t_X/\Delta t>1$ and the results obtained with $\Delta t_X=\Delta t$ is negligibly small. We note that in Eqs. (19)–(21), we kept $\Delta t_X=\Delta t$. In the next section, we provide the actual values of Δt_X and Δt for the chosen systems parameters and discuss in detail the accuracy of the simulations using the above approach.

C. Limiting case and validation of the 3D gLSM technique

To test the numerical accuracy and validate the above approach, we compared a solution obtained via our simulations with the numerical solution for a special, limiting case. If the sample is sufficiently small and the mobility of the polymer is sufficently high, the above system of equations [see Eqs. (1)–(3)] could be significantly simplified. In particular, we can neglect the contributions from diffusion in Eq. (3) and assume that the evolution of ϕ follows (is enslaved to) the changes in the reactant concentrations. The latter assumption means that the elastic stress is instantaneously equilibrated with the osmotic pressure, i.e., the following equation is valid at all times:

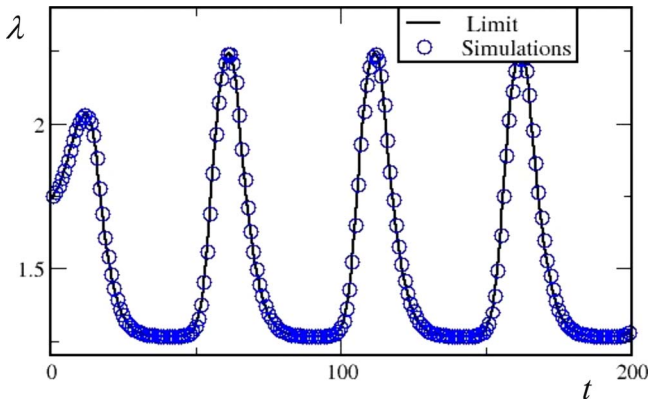

FIG. 2. (Color online) Evolution in time of the degree of swelling λ. The solid line shows the degree of swelling of the sample in the limiting case of no diffusion and instantenous pressure equilibration (corresponding numerical solution is obtained using MATHEMATICA™ software). The circles correspond to the simulations results obtained using the 3D gLSM model formulated above with $f=0.8$, $L_x=L_y=L_z=2$, and $\Lambda_0=10^3$. The initial conditions in both cases were chosen as follows: $v_{\mathrm{ini}}=0.185258$, $u_{\mathrm{ini}}=0.20931$, and $\lambda_{\mathrm{ini}}=1.73907$.

$$c_0 v_0\left[\left(\frac{\phi}{\phi_0}\right)^{1/3}-\frac{\phi}{2\phi_0}\right]=\pi_{osm}(\phi,v). \tag{22}$$

By solving Eq. (22), we obtain the concentration of the oxidized catalyst in this limiting case $v\equiv v_{\mathrm{lim}}$ as a function of the polymer volume fraction ϕ:

$$v_{\mathrm{lim}}=(\phi\chi^*)^{-1}\left\{c_0 v_0\left[\left(\frac{\phi}{\phi_0}\right)^{1/3}-\frac{\phi}{2\phi_0}\right]+\ln(1-\phi)+\phi+(\chi_0+\chi_1\phi)\phi^2\right\}. \tag{23}$$

Therefore, there are only two independent variables and, correspondingly, we need to solve only two independent evolution equations from the system of Eqs. (1)–(3). Thus, we find u and ϕ by solving the following system of equations:

$$\frac{d\phi}{dt}=\frac{\phi}{v_{\mathrm{lim}}(\phi)}\left[\frac{dv_{\mathrm{lim}}(\phi)}{dt}-\varepsilon\, G|_{v=v_{\mathrm{lim}}(\phi)}\right], \tag{24}$$

$$\frac{du}{dt}=-\frac{u}{1-\phi}\frac{d\phi}{dt}+F|_{v=v_{\mathrm{lim}}(\phi)}, \tag{25}$$

where v_{lim} is given by Eq. (23). By solving Eqs. (24) and (25) numerically with appropriate initial conditions, we find the temporal evolution of the volume fraction of the polymer in this limiting case $\phi_{\mathrm{lim}}(t)$ and, therefore, the degree of swelling $\lambda_{\mathrm{lim}}(t)=[\phi_0/\phi_{\mathrm{lim}}(t)]^{1/3}$.

The solid line in Fig. 2 shows the numerically obtained (via MATHEMATICA™ software) values for $\lambda_{\mathrm{lim}}(t)$, while the open circles show the data obtained from our 3D gLSM approach described above. In the gLSM simulations, the sample size was fixed at $2\times2\times2$, which is the smallest sample size considered here; the dimensionless kinetic coefficient was set to $\Lambda_0=10^3$. In addition, we set the simulation time steps to $\Delta t=10^{-3}$ and $\Delta t_X=5\times10^{-3}$, and used the same

parameters and initial conditions as used in solving Eqs. (24) and (25) (see caption to Fig. 2). The standard deviations between the simulation values and the values obtained in the limiting case via the MATHEMATICA™ software are $\approx 5 \times 10^{-3}$, which confirms the high accuracy of the proposed approach. (To obtain these standard deviation values, we averaged over simulation points taken at time increments equal to 1 within the time frame $t=0$ to $t=400$.) The presence of these small deviations reflects the fact that while we chose a high value for the polymer mobility (Λ_0), the chosen value is not sufficiently large to meet the underlying assumption in Eq. (22). To further test the accuracy of our approach, we increased the value of the dimensionless kinetic coefficient to $\Lambda_0=10^6$ and found that the standard deviation between the values obtained in simulations and the values obtained in the limiting case decreased to $\approx 3 \times 10^{-4}$. (The simulations with such high values of Λ_0 were conducted with the time steps of $\Delta t=10^{-5}$ and $\Delta t_X=5 \times 10^{-5}$.)

In the case of larger gel samples, the diffusion of u is essential, so we used other means to test the accuracy of our simulations. In particular, we varied the spatial discretization and compared results obtained at different discretizations. For the parameters and initial conditions given above (with $f=0.8$), we fixed the dimensionless linear size of the cubic sample in the undeformed state at $S=23$ and varied the spatial discretization by taking the length L of the cubic sample to be 12, 24, 48, and 60 nodes. The respective values of Δ, the length of the element's side in the undistorted state, were equal to 2.09, 1.00, 0.49, and 0.39. (Here, we calculate $\Delta = S/L$ for each value of L so that the actual size of the sample remains the same in all cases.) For all four simulations, we obtained the evolution of ϕ (averaged over all the elements). From data taken within a large time frame (from $t=500$ to 2500), we also calculated the period of oscillations τ and the time averaged value of polymer volume fraction $\langle \tilde{\phi} \rangle$ (see the definition below). The deviation of the values for τ and $\langle \tilde{\phi} \rangle$ obtained with $\Delta \approx 2.09$, $\Delta=1.0$, and $\Delta \approx 0.49$ from the corresponding values obtained with $\Delta \approx 0.39$ did not exceed 2, 0.4, and 0.05 %, respectively. In all the simulations presented below, we fixed $\Delta=1$, since this spatial discretization allowed us to calculate $\langle \tilde{\phi} \rangle$ and τ with a sufficiently high accuracy. In all simulations below, we specify the linear size of the cubic sample by stating the number of nodes in each direction L; with the above choice of $\Delta=1$, the linear dimensionless size of the sample in the undeformed state is $S=L-1$. And finally, in all the simulations below, we use $\Delta t=10^{-3}$ and $\Delta t_X=5 \times 10^{-3}$. The values of τ and $\langle \tilde{\phi} \rangle$ obtained with these Δt and Δt_X only deviated from values obtained with $\Delta t_X=\Delta t=10^{-3}$ by at most 0.005%.

III. RESULTS AND DISCUSSION

In our simulations, we observe that behavior of the gel depends on the size of the sample. To facilitate the discussion, we first show the graphical output from our 3D gLSM simulations that illustrates the regular oscillations of a BZ gel; the size of the sample is $12 \times 12 \times 12$ (see Fig. 3) [34]. In this and the following simulations, we imposed the no-flux boundary conditions at the surface of the sample (unless specified otherwise). The snapshots in Fig. 3 are taken during one period of oscillation at late times to ensure that the simulations capture the regular, nontransient behavior. Within these images, the black lines mark the elements and the colors represent the concentration of oxidized catalyst v with the color bar given in Fig. 3(g). (The same color scheme is used throughout this section, however, the values of $v_{\min}$ and $v_{\max}$ are different in each of the figures and are specified in the respective figure captions.)

The least swollen sample [Fig. 3(a)] corresponds to the lowest concentration of oxidized catalyst v. (In the color bar, yellow corresponds to values close to $v_{\min}$.) As the concentration of oxidized catalyst increases in the course of BZ reaction, the sample's degree of swelling also increases, as shown in Figs. 3(b)–3(d). Correspondingly, when v begins to decrease, the degree of swelling also decreases, as illustrated in Figs. 3(e) and 3(f). This is similar to the in-phase sinchronization of chemical and mechanical oscillations observed experimentally by Yoshida *et al.* in cubic gel pieces that were smaller than the characteristic length scale of the chemical wave [18].

As initial conditions for the above simulations, we chose the concentrations of the oxidized catalyst and reagent u to be randomly distributed around their stationary solutions v_{st} and u_{st}, respectively [see Eq. (13) above] [35]. Initially, each element was taken to be a cube with side $\lambda_{st}\Delta$, where λ_{st} was defined by the value of the stationary solution for the polymer volume fraction ϕ_{st} [see Eq. (13)]. We note that we examined the evolution of the system with different initial conditions (for example, significantly decreasing and increasing the size of the cubic element) and confirmed that the late-time oscillations were always identical to the ones shown in Fig. 3. Thus, for a fixed set of materials parameters and sample size, the oscillations presented in Fig. 3 do not depend upon the initial conditions.

In Fig. 4, we plot the evolution of $\langle u \rangle$, $\langle v \rangle$, and $\langle \phi \rangle$, which are the respective average values of the concentrations of the reagents, oxidized catalyst and polymer volume fraction, for the sample shown in Fig. 3. The average values are taken over all the elements within the sample at each moment of time. The dots marked $(a)-(f)$ correspond to the images in Fig. 3, $(a)-(f)$. In this figure, τ marks the period of oscillations, and $\delta=\langle \phi \rangle_{\max}-\langle \phi \rangle_{\min}$ marks the amplitude of the oscillation of $\langle \phi \rangle$. In addition, we define $\langle \tilde{\phi} \rangle$ as the average value of $\langle \phi \rangle$ around which the system oscillates in time, i.e., $\langle \tilde{\phi} \rangle = (\langle \phi \rangle_{\max}+\langle \phi \rangle_{\min})/2$, where $\langle \phi \rangle_{\max}$ and $\langle \phi \rangle_{\min}$ are the respective maximum and minimum values of $\langle \phi \rangle$ calculated at late times when the oscillations are regular. We use the values of $\langle \tilde{\phi} \rangle$ and τ to quantitatively characterize the system undergoing regular, periodic oscillations.

To gain insight into the dependence of the dynamical behavior on the size of the sample, we next studied the dynamics of a sample of size $24 \times 24 \times 24$; all other parameters were kept the same as in Fig. 3. The snapshots in Fig. 5 show the sample's evolution at late times and reveal that the oscillations are irregular. Moreover, the actual realization of the dynamic pattern depends on the small random fluctuations in

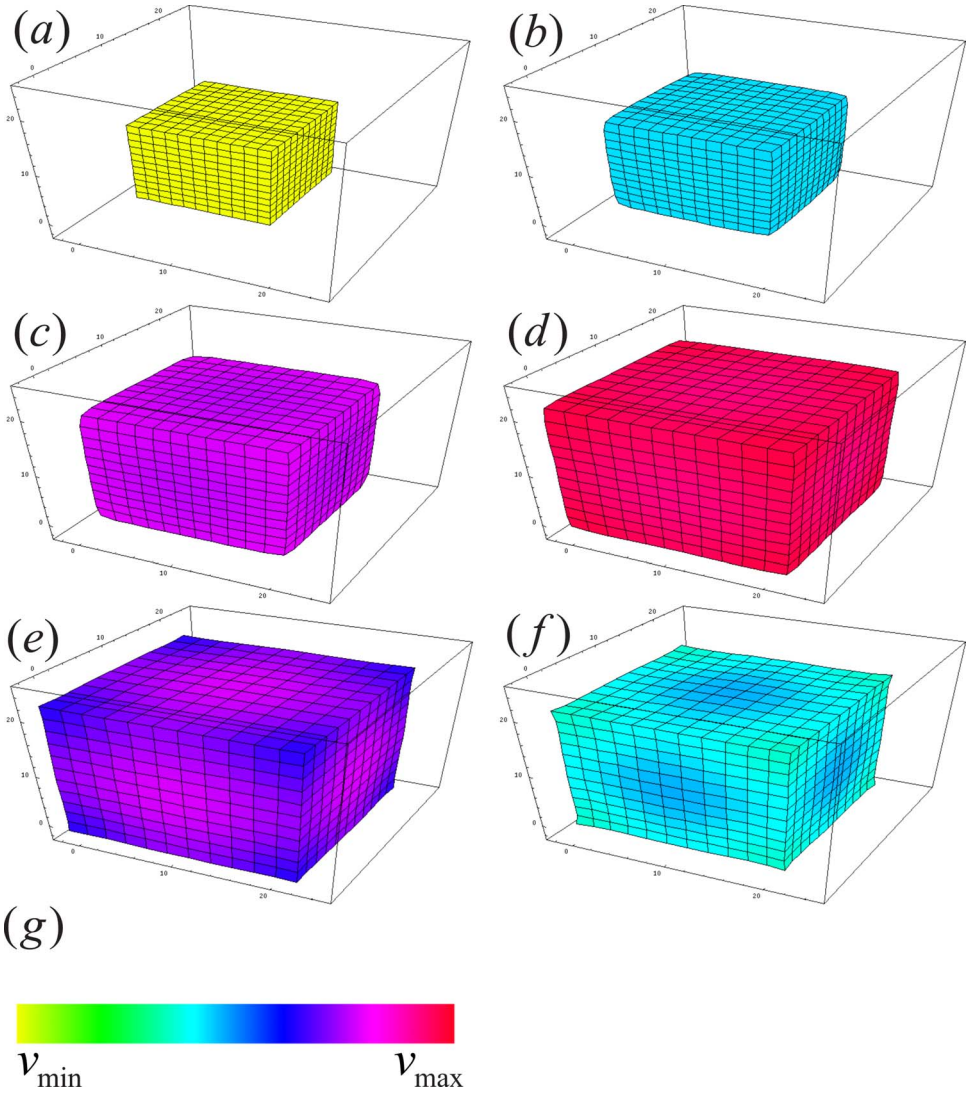

FIG. 3. (Color online) Regular oscillations in reactive chemoresponsive gel. The size of the sample is $12\times12\times12$ and the stoichiometric factor in BZ reaction is $f=0.68$. Corresponding simulation times are (a) 1761, (b)1770, (c) 1773, (d) 1776, (e)1785, (f) 1788. The minimum and maximum values for the color bar are $v_{min}=8\times10^{-4}$ and $v_{max}=0.4166$, respectively. [We note that we use the same color bar, (g), in all the following images, whereas the values of v_{min} and v_{max} are given separately for each figure.]

the initial conditions. What we observe is analogous to a fragment of a spiral wave that is typically observed in BZ reactive systems and the originating point for this wave depends on the small random fluctuations in the initial conditions of the system. If, however, we increase the value of the stoichiometric factor from $f=0.68$ (in Figs. 3–5) to $f=0.9$, then the gel sample is observed to exhibit the regular periodic oscillations, as shown in Fig. 6.

The above examples illustrate that the behavior of the system drastically depends on both the stoichiometric factor f, which is an adjustable parameter of the model, and on the size of the sample. In the following simulations, we vary f in the range from 0.4 to 0.95. (The values of f are increased in increments of 0.05 except in regions close to the critical points, where we reduced these increments to 0.01 in order to more precisely define the critical values f^* and f^{**}.) Furthermore, we conducted these simulations for four different sample sizes $L\times L\times L$ (with $L=2$, 6, 12, and 24). For each

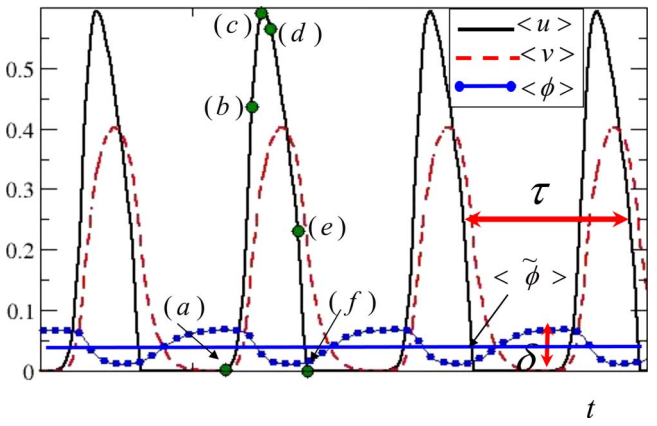

FIG. 4. (Color online) Evolution of $\langle u\rangle$, $\langle v\rangle$, and $\langle\phi\rangle$ for the sample shown in Fig. 3. Here, τ marks the period of oscillations, δ marks the amplitude of oscillation of $\langle\phi\rangle$ and $\langle\tilde{\phi}\rangle$ marks its average value.

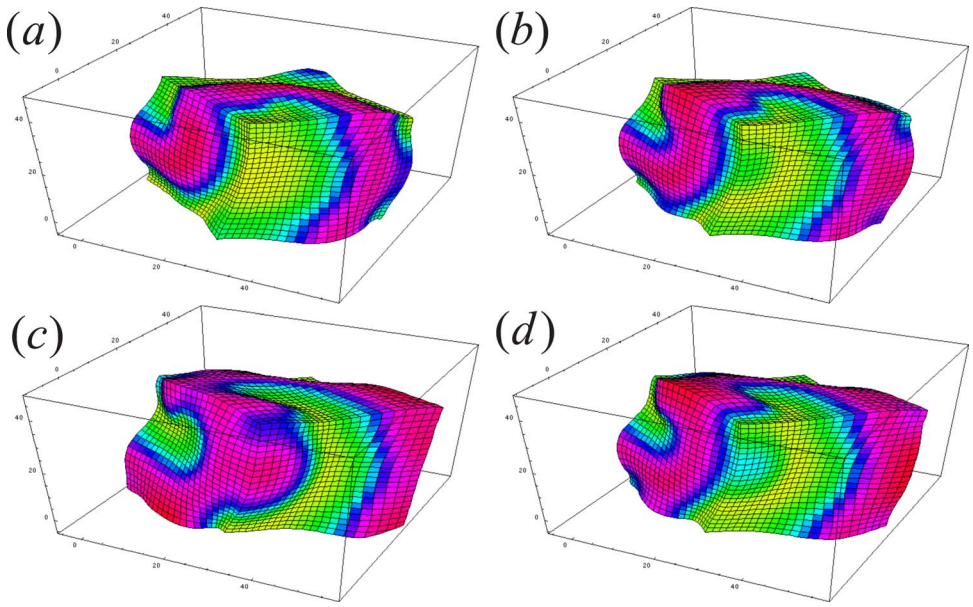

FIG. 5. (Color online) Nonregular oscillations in a reactive chemoresponsive gel. The size of the sample is $24\times24\times24$ and the stoichiometric factor in BZ reaction is $f=0.68$. Corresponding simulations times are (a) 1761, (b)1764, (c) 1771, (d) 1797. The minimum and maximum values for the color bar [given in Fig. 3(g)] are $v_{\min}=7\times10^{-3}$ and $v_{\max}=0.4342$, respectively.

value of f and L, we ran three independent simulations with different random perturbations in the initial conditions. Each of these simulations was run for a sufficiently long time (until $t=2000$) to ensure that the observed behavior is nontransient and robust for the given set of parameters. We note that the case with $L=2$ (i.e., the dimensionless linear size of the sample is 1 in the undeformed state) corresponds to a sample size that is much smaller than the characteristic diffusion length in the system. The findings from this series of simulations are summarized in Fig. 7. For the samples undergoing regular oscillations, we plot the average value of the polymer volume fraction $\langle\tilde{\phi}\rangle$ around which the system oscillates in time (as defined above). For the nonoscillatory systems, we plot the average value of the polymer volume fraction $\langle\phi\rangle$ that the system reaches at late times (because this value remains constant at late times, $\langle\phi\rangle=\langle\tilde{\phi}\rangle$). The black dashed curve represents a stationary solution $\phi_{\rm st}$ of Eq. (13). The value of $\langle\phi\rangle$ in each of the elements reaches its stationary value $\phi_{\rm st}$, when the system is in the nonoscillatory regime, i.e., when $f\leqslant f_L^*$, where f_L^* is the critical value of the stoichiometric factor. In these cases, $\langle\phi\rangle$ is equal to the respective value of $\phi_{\rm st}$ taken at each f and does not depend on the size

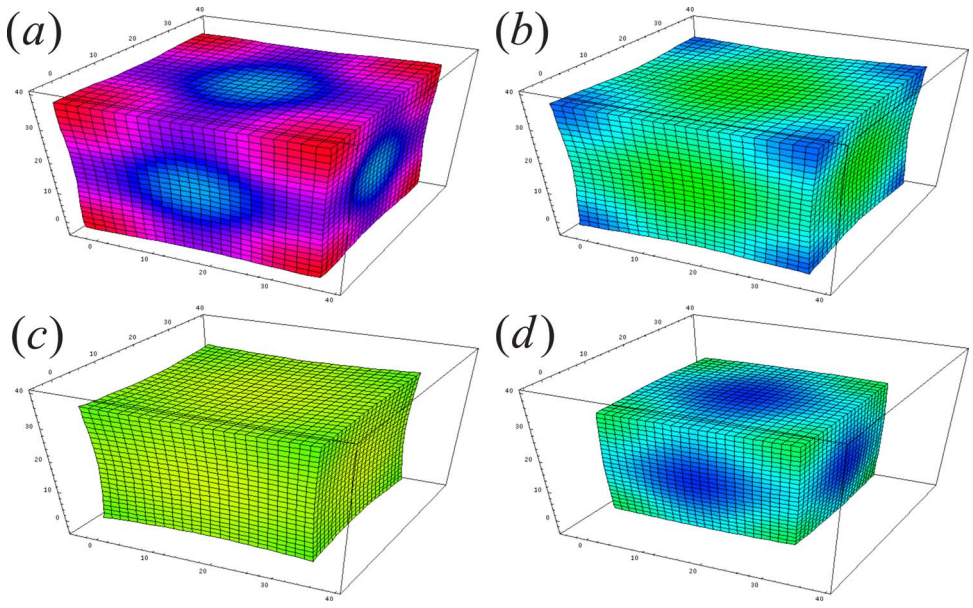

FIG. 6. (Color online) Effect of increasing the value of the stoichiometric factor in BZ reaction on the dynamics of the sample. Here, $f=0.9$ and all other papameters are the same as in Fig. 5. Corresponding times are (a) 1761, (b)1764, (c) 1770, (d) 1797. The minimum and maximum values for the color bar [given in Fig. 3(g)] are $v_{\min}=3\times10^{-4}$ and $v_{\max}=0.2470$, respectively.

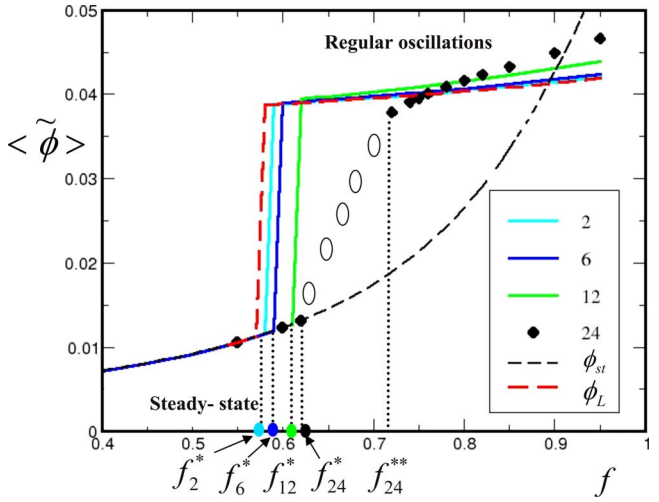

FIG. 7. (Color online) Phase behavior for the gel samples of various sizes. The sizes of the samples ($L \times L \times L$) are provided in the legend; here we choose $L=2,6,12$ (solid lines) and $L=24$ (diamonds). Gray dashed line (red online) marked ϕ_L represents solution in the limiting case (no diffusion and ϕ is instantaneously enslaved to the changes in reactant concentration).

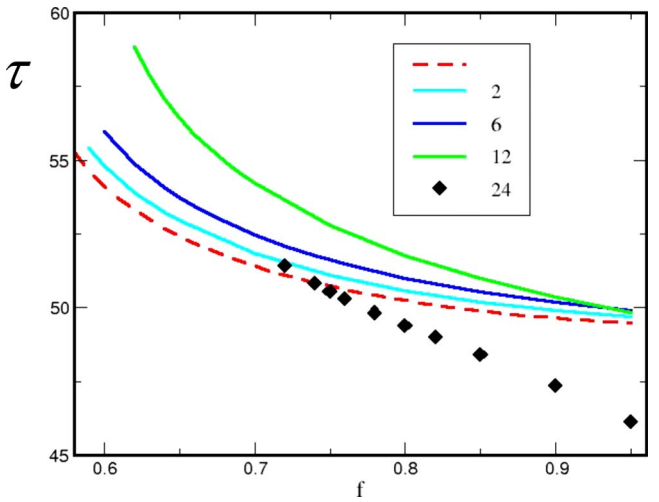

FIG. 8. (Color online) Period of oscillations for the gel samples of various sizes. The sizes of the samples ($L \times L \times L$) are provided in the legend (we choose $L=2$, 6, 12, and 24). Gray dashed line (red online) marked ϕ_L represents solution in the limiting case (no diffusion and ϕ is instantaneously enslaved to the changes in reactant concentration).

of the sample. In other words, the black dashed line corresponding to ϕ_{st} coincides with the lines connecting simulation data points for each of the values of L if $f \leqslant f_L^*$ (see Fig. 7).

The above results reveal a rather notable phenomenon: increasing the size of the sample increases the critical value of f_L^* (for the range of sizes and the no-flux boundary conditions considered here). Thus, for example, a sample with $L=2$ will exhibit oscillatory behavior at a lower value of f than a sample with $L=12$. Consequently, if we consider a system that encompasses gel samples of different sizes and the stoichiometric factor is set at $f=f_{12}^*$, then all samples with a size smaller than $L=12$ will undergo regular, nondecaying oscillations, while all samples with $L \geqslant 12$ can undergo transient oscillation, but at late times will always reach the steady state. This implies that by decreasing the size of the sample (while keeping no-flux boundary conditions for u on the surface of the sample), one can induce transitions from the nonoscillatory to oscillatory regime.

Figure 7 also reveals that for the samples with $L \leqslant 12$, only one critical value $f_L^*(L)$ is observed in the simulations, so that if $f > f_L^*(L)$, we observe regular oscillations of the sample [36]. On the contrary, for the gel samples of larger sizes ($L=24$ in Fig. 7), the simulation results yield two critical values f_{24}^* and f_{24}^{**}. For $f \leqslant f_{24}^*$, the system reaches a steady state at late times and for $f \geqslant f_{24}^{**}$, we observe the regular oscillations. For $f_{24}^* < f < f_{24}^{**}$, however, the gel sample undergoes nonregular oscillations; an example of this behavior is shown in Fig. 5. The open circles in Fig. 7 simply indicate the general region of the nonregular oscillations for the sample with $L=24$ because the calculation of $\langle \tilde{\phi} \rangle$ (as defined above) only applies to regular oscillations. We note that additional simulations showed that the region of nonregular oscillations also exists for samples of sizes $L=18$ and 36.

Finally, the gray dashed line in Fig. 7 (red online) corresponds to the limiting case of a small sample with no diffusion and an instantaneous pressure equilibration (see Sec. II C). As we discussed above, we recover this limiting case in our simulations by setting $L=2$ and taking a sufficiently high value for the dimensionless kinetic coefficient Λ_0. For the simulations in Fig. 7, we set $\Lambda_0=10^2$, and it is for this reason that the transition point between the steady-state and the oscillatory regime for $L=2$ is shifted to a higher f relative to the transition in the limiting case. If, however, we increase the mobility to $\Lambda_0=10^3$ or higher, the transition line coincides with the gray dashed line shown in Fig. 7 (red online). In other words, a decrease in the mobility of the polymer results in an increase in the value of f^*, so that the sample with the higher Λ_0 has a larger oscillatory region. (We confirmed the latter statement by considering samples with even smaller values of $\Lambda_0=10$ and $\Lambda_0=1$).

We note that for all of the cases of regular oscillations, if the value of f is close to its critical value above which the regular oscillations occur (i.e., f_L^* for the smaller sized samples and f_L^{**} for the larger samples), the average value of the polymer volume fraction around which system oscillates $\langle \tilde{\phi} \rangle$ is significantly larger than the value corresponding to the steady-state solution ϕ_{st}. In other words, if we increase the value of f, the sample becomes much more compressed on average when the oscillation occurs than when the sample is in the steady state.

In Fig. 8, for all cases of regular oscillations, we plot the dependence of the period of oscillation τ on the value of f. Again, the gray dashed line (red online) corresponds to the solution in the limiting case as defined in Sec. II C and all the simulation data are represented in the same way as in Fig. 7. [If we increase the mobility of the polymer so that $\Lambda_0=10^3$ (or higher) at $L=2$, we recover the gray dashed line (red online) in Fig. 8.] Figure 8 illustrates that for all sample

sizes considered here, an increase in f results in a decrease in the period of oscillations. For a fixed value of f, however, the dependence of the period on the sample size is more complicated. Figure 8 shows that for the smaller samples ($L=2$, 6, and 12), an increase in size results in an increase in τ (at fixed f). This increase is more apparent at the lower values of f within the oscillatory regime, and becomes smaller as the value of f increases. At the highest values of f considered here, the periods of oscillation for all the samples of small sizes ($L=2$, 6, and 12) are approximately equal and are close to the value obtained in the limiting case for the same f. If, however, we further increase the size of the sample ($L=24$ in Fig. 8), the period of oscillation becomes smaller than that of the smaller samples at fixed f (see black diamonds in Fig. 8). Such significant changes in τ could be attributed to the propagation of traveling waves throughout the sample.

Some aspects of the size effect on the dynamical behavior of BZ gel are similar to features observed experimentally for spherical, nonresponsive gel beads undergoing the BZ reaction [37]. In particular, the researchers observed [37] a switching between the "global rhythm" and "traveling wave" regimes of chemical oscillations as they increased the size of the spherical bead. For smaller bead sizes, they observed so-called "global oscillations," where the reactant concentrations at each moment of time were almost uniform throughout the sample. This is similar to what we observe for the small sample sizes, where diffusion is relatively unimportant (i.e., for $L \leqslant 12$). While for $L=12$ the concentrations of the reactants are somewhat nonuniform (as can be seen from Fig. 3), the effect of diffusion still remains small, i.e., in the above context, the oscillations can be regarded as "rhythmic." For the larger bead sizes, they observed traveling chemical waves within the sample [37]; this is again similar to what we observe for relatively large values of L, such as for $L=24$ in the simulations above. Finally, these researchers also demonstrated [37] that the frequency of oscillations is higher for the cases of the traveling waves than for the cases of rhythmic oscillations. This observation is analogous to what we observe in Fig. 8, where the period of oscillations is smaller for $L=24$ (i.e., the case where we clearly observe traveling waves propagating throughout in the sample).

In the next series of simulations, we fix $f=0.8$ and $L=12$, but vary the value of ε. We note that the value of ε is proportional to the concentration of the organic species in the BZ reaction (see the definition of the dimensionless value of ε given in Ref. [12]). More specifically, with respect to the experiments in Refs. [15–20], ε is proportional to the concentration of the malonic acid (MA). Figure 9(a) illustrates the evolution of the average degree of swelling for the samples with $\varepsilon=0.04$ and 0.1. The plot shows that the period of oscillations dramatically decreases with the increase in ε. This trend is also illustrated in Fig. 9(b), where we plot the period of oscillations for a range of ε. The decrease in the period of oscillations with an increase in ε that is observed in the simulations is in a qualitative agreement with the experimental results of Yoshida *et al.* [18–20]. Finally, if we further increase the value of ε (i.e., $\varepsilon \geqslant 0.9$ for the scenario presented above), we observe a transition to the nonoscillatory regime; this observation also agrees qualitatively with experimental studies [20] where researchers observed a transition between the oscillatory and nonoscillatory regimes with an increase of concentration of MA.

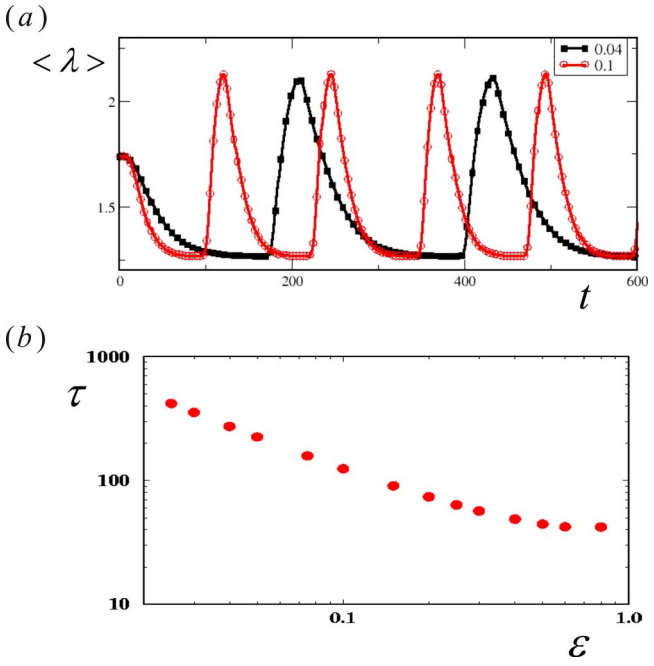

FIG. 9. (Color online) Effect of varying ε on the dynamics of the sample with $L=12$ and $f=0.8$. (a) Evolution in time of the degree of swelling, λ, for $\varepsilon=0.04$ and 0.1 as marked in the legend, respectively. (b) Dependence of the period of oscillations τ on ε.

Finally, we show that the dynamics of a gel sample depends remarkably on the boundary conditions at the surface of the sample. As we noted, in all the simulations presented above, we applied the no-flux boundary conditions for the dissolved reactant u at the surface of the samples. Such no-flux boundary conditions correspond, for example, to the scenario where the entire sample is placed in an impermeable but very elastic and flexible casing, which does not permit a flux of reagents in or out of the gel. We can consider another limiting case; namely, the concentration of u is kept at $u=0$ outside of the sample and, therefore, there is a diffusive flux of u through the surface of sample into the outer solution. (To keep $u=0$ in this outer solution, one should continuously remove the reactant u from the solution, as in the continuously stirred tank reactors.)

Figures 10(a)–10(c) shows snapshots of the time evolution of a sample with $u=0$ in the outer solution and with a diffusive flux of u through the surface of the sample. The images in the left column show the distribution of v within the entire sample, and the images in the right column show the distribution of v in the planes that cross through the center of the sample (i.e., the images on the right allow us to look "inside" the images on the left). The simulations show that sample exhibits regular oscillation, which can be seen from the temporal evolution of the average swelling of the sample [see the solid black line in Fig. 10(d)]. All the system parameters (including the initial conditions and the sample size) are identical to those in Fig. 5; the only difference between the gel samples in Figs. 5 and 10 is the boundary conditions. The evolution of the average swelling of the

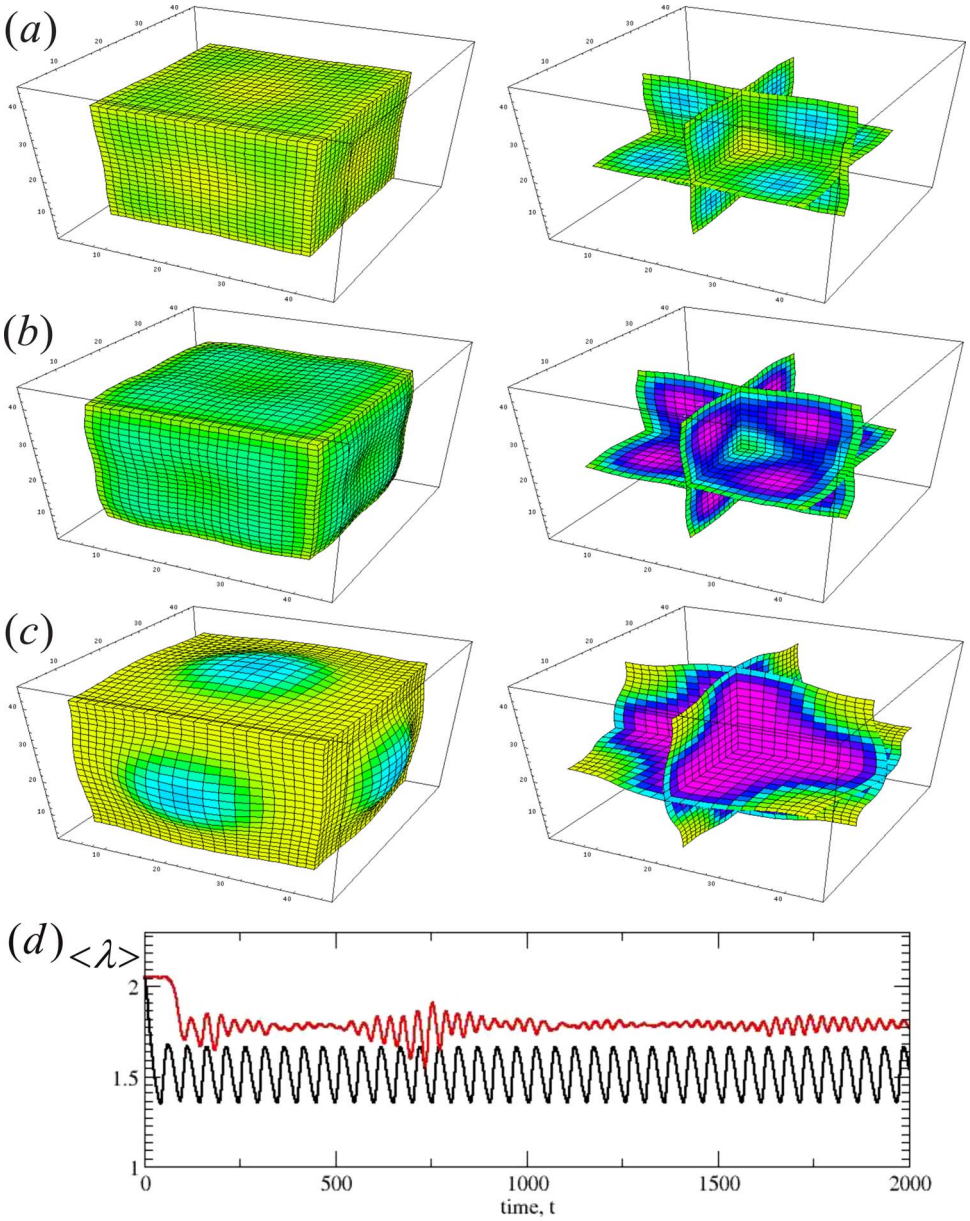

FIG. 10. (Color online) Effect of the flux through the surface of the sample (a)–(c). Evolution of the sample at simulation times (a) 1770, (b) 1773, (d) 1791. Values for the color bar [given in Fig. 3(g)] are $v_{min}=6\times10^{-5}$ and $v_{max}=0.3728$. (d) Evolution of the average degree of swelling of the sample in Fig. 5 (gray line) (red online) and in Figs. 10(a)–10(c) (black line).

sample in Fig. 5 is also shown in Fig. 10(d) by the solid gray line (red online).

Figure 10(d) illustrates that the sample with the no flux boundary condition undergoes nonregular oscillation and has a significantly higher degree of swelling than the sample with the diffusive flux through its boundary. More specifically, in the case shown in Fig. 10, the diffusion of u through the surface of the sample creates a gradient of u in the vicinity of the sample's surface. This gradient, in turn, causes a decrease in value of the oxidized catalyst v and, therefore, an effective shrinking of the gel close to the surfaces in the sample. In other words, even though the initial size of the samples in Figs. 10 and 5 were chosen to be equal and the number of nodes was kept fixed at $24\times24\times24$, the actual average size in Fig. 10 is smaller than in Fig. 5, contributing to the fact that the oscillations of the sample become regular.

The simulations discussed above illustrate that the type of oscillations observed in the system, as well as the period and the amplitude of these oscillations, depend strongly on the boundary conditions at the surface of the sample. This fact could potentially open up possibilities for controlling the oscillation of the gel by simply changing the concentration of u in the outside solution.

IV. CONCLUSIONS

We developed an efficient computational approach for capturing the complex three-dimensional behavior of chemo-responsive polymer gels undergoing the Belousov-Zhabotinsky reaction. This computational model combines

components of the finite difference and finite element techniques and is an extension to a third dimension of the recently developed two-dimensional gLSM model [11,12].

Using this approach, we observed different types of dynamic behavior in this nonlinear system. In particular, we found that for sufficiently large samples with no-flux boundary conditions (for the dissolved BZ reactant on the surface of the sample), both regular and nonregular oscillations in the size and shape of the sample can occur depending on the value of the reaction parameters. For smaller sized samples, however, we only observed regular oscillations or a nonoscillatory state.

From our simulations, we isolated critical values of the stoichiometric factor at which the transitions between different types of behavior (regular or nonregular oscillations or nonoscillatory regime) occur in the cubic gel sample with the no-flux boundary conditions at the surface. We found that these critical values depend on the size of the sample. For example, increasing the size of the sample increases the critical value of f_L^* that corresponds to the transition between the nonoscillatory and oscillatory regimes for a sample of size L. Thus, if one considers a system that encompasses a number of gel samples of different sizes and the stoichiometric factor is set at $f=f_L^*$, then all the samples of a size smaller than L will undergo regular, nondecaying oscillations, while all the samples of a size equal to or larger than L will always reach the steady state. This behavior also implies that by decreasing the size of the sample (for example, by cutting the sample onto smaller pieces), one can induce transitions from the nonoscillatory to the oscillatory regime.

We also examined the oscillations of a cubic gel for two different types of boundary conditions on the surface on the sample: in one scenario, we applied no-flux boundary conditions on the dissolved reactant and in the other scenario, we took into account the flux of the reactant through the surface of the sample into the outside solution. Our results reveal that the dynamics and pattern formation in the BZ gels dramatically depend on the boundary conditions at the sample's surface. These effects could potentially open up possibilities for controlling the oscillations of the gel by simply changing the concentration of the reagents in the outside solution.

The findings from our simulations yield significant insight into the factors that govern the dynamics of these self-oscillating BZ gels. We note that the autonomous behavior of the BZ gels provides distinct opportunities for designing smart, biomimetic systems and devices that can effectively operate without the use of any external stimuli [38]. To fully harness the unique properties of these gels, we need fundamental studies to identify the critical parameters that control their properties; the 3D gLSM model developed here could be an important tool for conducting such studies. Ultimately, such fundamental studies would allow us to not only design self-actuating or self-propelled gel-based systems, but also establish guidelines for maximizing the efficiency and performance of these unique systems.

ACKNOWLEDGMENTS

The authors gratefully acknowledge financial support from ARO.

APPENDIX

1. Definitions of shape functions and integrals within element needed to formulate 3D gLSM model

Within each element, we define a local coordinate system (ξ,η,ζ) as shown in Fig. 1(a). The local coordinates within the element $\mathbf{m}$ can be calculated as [31,32]

$$\mathbf{r}(\mathbf{m}) = \sum_{n=1}^{8} N_n \mathbf{r}_n(\mathbf{m}), \tag{A1}$$

where $\mathbf{r}_n(\mathbf{m}) \equiv (x_n(\mathbf{m}), y_n(\mathbf{m}), z_n(\mathbf{m}))$ gives the coordinates of node n of the given element $\mathbf{m}$. The N_n are shape functions defined as $N_n = \frac{1}{8}(1+\xi\xi_n)(1+\eta\eta_n)(1+\zeta\zeta_n)$, where ξ_n, η_n, and ζ_n are constants equal to ± 1, depending on the node n. Specifically, for the node numbering in Fig. 1, the shape functions have the following explicit form [31]:

$$N_1 = \frac{1}{8}(1-\xi)(1-\eta)(1-\zeta), \quad N_2 = \frac{1}{8}(1-\xi)(1-\eta)(1+\zeta),$$

$$N_3 = \frac{1}{8}(1+\xi)(1-\eta)(1+\zeta), \quad N_4 = \frac{1}{8}(1+\xi)(1-\eta)(1-\zeta),$$

$$N_5 = \frac{1}{8}(1-\xi)(1+\eta)(1-\zeta), \quad N_6 = \frac{1}{8}(1-\xi)(1+\eta)(1+\zeta),$$

$$N_7 = \frac{1}{8}(1+\xi)(1+\eta)(1+\zeta), \quad N_8 = \frac{1}{8}(1+\xi)(1+\eta)(1-\zeta). \tag{A2}$$

In terms of the local coordinates (ξ,η,ζ), the positions of the faces of the element are defined as $\xi=\pm 1$, $\eta=\pm 1$, and $\zeta=\pm 1$.

The volume of the element $\mathbf{m}$ can be found by integrating over the local coordinates as

$$V(\mathbf{m}) = \int_{-1}^{1}\int_{-1}^{1}\int_{-1}^{1} \det J(\mathbf{m}) d\xi d\eta d\zeta, \tag{A3}$$

where J is the Jacobian matrix [31,32]

$$J(\mathbf{m}) = \begin{bmatrix} \partial x(\mathbf{m})/\partial\xi & \partial y(\mathbf{m})/\partial\xi & \partial z(\mathbf{m})/\partial\xi \\ \partial x(\mathbf{m})/\partial\eta & \partial y(\mathbf{m})/\partial\eta & \partial z(\mathbf{m})/\partial\eta \\ \partial x(\mathbf{m})/\partial\zeta & \partial y(\mathbf{m})/\partial\zeta & \partial z(\mathbf{m})/\partial\zeta \end{bmatrix}. \tag{A4}$$

In order to calculate $\mathbf{n}_{i(\text{face})}(\mathbf{m}')S_{i(\text{face})}(\mathbf{m}')$ for the face i(face) of the element $\mathbf{m}'$, we calculate the area of this face in the local coordinate system using the above definitions of the shape functions. For example, for face 1 (which is the bottom face comprising the nodes 1,5,8, and 4 in Fig. 1), we calculate $\mathbf{n}_1(\mathbf{m})S_1(\mathbf{m})$ as [32]

$$\mathbf{n}_1(\mathbf{m})S_1(\mathbf{m}) = \left\{\int_{-1}^{1}\int_{-1}^{1}\begin{Bmatrix}\partial x(\mathbf{m})/\partial\xi\\ \partial y(\mathbf{m})/\partial\xi\\ \partial z(\mathbf{m})/\partial\xi\end{Bmatrix} \times \begin{Bmatrix}\partial x(\mathbf{m})/\partial\eta\\ \partial y(\mathbf{m})/\partial\eta\\ \partial z(\mathbf{m})/\partial\eta\end{Bmatrix} d\xi d\eta\right\}\Bigg|_{\zeta=-1}, \quad \text{(A5)}$$

where we took into account that the position of the face 1 corresponds to $\zeta=-1$ in the local coordinate system.

2. Calculations of springlike force $\mathbf{F}_{1,n}(\mathbf{m})$ acting on node n of element $\mathbf{m}$

To obtain $\mathbf{F}_{1,n}(\mathbf{m})$, we calculate the contribution $U_1 = c_0 v_0 I_1/2$ from the elastic energy of the deformed elements, and then differentiate the result with respect to $\mathbf{r}_n(\mathbf{m})$. If all the coordinates of all the nodes of the element $\mathbf{r}_n(\mathbf{m})$ are known, the first invariant of the strain tensor can be written in the local coordinate system for this element $\mathbf{m}$ as

$$I_1[\xi,\eta,\zeta,\mathbf{r}(\mathbf{m})] = \frac{4}{\Delta^2}\left[\sum_{n=1}^{8}\left(\mathbf{r}_n(\mathbf{m})\frac{\partial N_n}{\partial\xi}\right)^2 + \sum_{n=1}^{8}\left(\mathbf{r}_n(\mathbf{m})\frac{\partial N_n}{\partial\eta}\right)^2 + \sum_{n=1}^{8}\left(\mathbf{r}_n(\mathbf{m})\frac{\partial N_n}{\partial\zeta}\right)^2\right]. \quad \text{(A6)}$$

It can be shown that the exact integration over the volume of the element $\mathbf{m}$ in the local coordinate system for this element gives the contribution from the above term to the elemental energy density in the following form:

$$U_1(\mathbf{m}) = \frac{c_0 v_0}{16}\int_{-1}^{1}\int_{-1}^{1}\int_{-1}^{1} I_1[\xi,\eta,\zeta,\mathbf{r}(\mathbf{m})]d\xi d\eta d\zeta = \frac{c_0 v_0}{24\Delta^2}\left(\sum_{NN}[\mathbf{r}_n(\mathbf{m}) - \mathbf{r}_{n'}(\mathbf{m})]^2 + \sum_{NNN}[\mathbf{r}_n(\mathbf{m}) - \mathbf{r}_{n'}(\mathbf{m})]^2\right). \quad \text{(A7)}$$

In the equation above, Σ_{NN} represents a summation over all the next-nearest-neighbor nodal pairs (n,n'), and Σ_{NNN} represents a summation over all the next-next-nearest-neighbor nodal pairs (n,n') within the element $\mathbf{m}$. For the element shown in Fig. 1, Σ_{NN} represents a summation over the pairs (n,n') taking the following values: (2,7), (3,6),(4,7), (3,8), (2,5), (1,6),(1,3),(2,4), (4,5), (1,8), (6,8), (7,5), and Σ_{NNN} represents the summation over the pairs (n,n') taking the values (3,5), (4,6), (1,7), and (2,8). We note that the contributions from the interactions between the next-nearest-neighbor nodes and next-next-nearest-neighboring nodes have the same weight. Thus, the first term on the right-hand side of Eq. (A7) is effectively approximated by the elastic energy stored in the linear springs connecting next-nearest and next-next-nearest neighbor nodes, with the spring constant being the same for all the springs.

3. Calculations of the terms $T_0(\mathbf{m})$, $T_1(\mathbf{m})$, and $T_2(\mathbf{m})$ in Eqs. (20) and (21)

The term $T_0(\mathbf{m})$ in Eqs. (20) and (21), approximates the value of $\nabla\cdot\mathbf{v}^{(p)}$ calculated within the element $\mathbf{m}$; we calculate this term as

$$T_0(\mathbf{m}) = [1 - \phi(\mathbf{m},t+\Delta t)/\phi(\mathbf{m})]/\Delta t, \quad \text{(A8)}$$

where the values $\phi(\mathbf{m})$ and $\phi(\mathbf{m},t+\Delta t)$ are calculated using Eq. (14) based on the values of the $\mathbf{r}_n(\mathbf{m})$ at the times t and $t+\Delta t$, respectively.

The terms $T_1(\mathbf{m})$ and $T_2(\mathbf{m})$ in Eq. (21) correspond to the respective second and the third terms in Eq. (3) calculated within the element $\mathbf{m}$. In order to calculate $T_1(\mathbf{m})$, we integrate the corresponding term in Eq. (3) over the volume of the element, and then normalize the obtained value by the volume of this element:

$$T_1(\mathbf{m}) = \frac{1}{V(\mathbf{m})}\int_{\mathbf{r}\in V(\mathbf{m})} d\mathbf{r}\,\nabla\cdot\left[\mathbf{v}^{(p)}(\mathbf{m})\frac{u(\mathbf{m})}{1-\phi(\mathbf{m})}\right] = \frac{1}{V(\mathbf{m})}\sum_{i\ (\text{face})=1}^{6} \times \int dS_{i\ (\text{face})}\mathbf{n}_{i\ (\text{face})}\cdot[\mathbf{v}^{(p)}(\mathbf{m})\tilde{u}(\mathbf{m})]_{i\ (\text{face})}. \quad \text{(A9)}$$

Here, $\mathbf{n}_{i(\text{face})}(\mathbf{m})$ is the outward normal to the i(face) of the element $\mathbf{m}$, and $S_{i(\text{face})}$ is the area of this face. In Eq. (A9), we introduced the normalized concentration of the dissolved reagent as $\tilde{u}(\mathbf{m}) = u(\mathbf{m})[1-\phi(\mathbf{m})]^{-1}$. We note that the values of the polymer velocity $\mathbf{v}^{(p)}(\mathbf{m})$ are given only at the nodes of the element, while the values of the $\tilde{u}(\mathbf{m})$ are defined within the element $\mathbf{m}$. In order to calculate the integral over the surface of the element $\mathbf{m}$ on the right-hand side of Eq. (A9), we again integrate in the coordinate system local to this element using the shape functions as given above. Using the values of the polymer velocity $\mathbf{v}_n^{(p)}(\mathbf{m})$ defined at the nodes of the element, we can calculate the values of the product $\mathbf{v}^{(p)}(\mathbf{m})\tilde{u}(\mathbf{m})$ in Eq. (A9) within the element $\mathbf{m}$ as

$$\mathbf{v}^{(p)}(\mathbf{m})\tilde{u}(\mathbf{m}) = \sum_{n=1}^{8} N_n \mathbf{v}_n^{(p)}(\mathbf{m})\langle\tilde{u}(\mathbf{m})\rangle_n, \quad \text{(A10)}$$

where $\langle\tilde{u}(\mathbf{m})\rangle_n$ denotes the value of the $\tilde{u}(\mathbf{m})$ at the node n of the element $\mathbf{m}$; to calculate this value, we take an average value of the $\tilde{u}(\mathbf{m}')$ over all the neighboring elements $\mathbf{m}'$ that include the node n of the element $\mathbf{m}$. Also, we use the shape functions to write the $dS_{i(\text{face})}(\mathbf{m})\mathbf{n}_{i(\text{face})}(\mathbf{m})$ for each of the faces of the element [i(face) denotes the face number]. For example, $dS_1(\mathbf{m})\mathbf{n}_1(\mathbf{m})$ is already provided above and is the expression under the integral in Eq. (A5) taken at the bottom face (see Fig. 1), i.e., at $\zeta=-1$. With all the above, the integral in the right-hand-side of Eq. (A10) can be calculated with no further approximations. We do not provide the final expression here since it is cumbersome, but we note that we use the MATHEMATICA™ software package to obtain this expression and to convert it into our numerical code.

Finally, we approximate the term $T_2(\mathbf{m})$ in Eq. (21), which accounts for the diffusion of u in the gel matrix, as

$$T_2(\mathbf{m}) = \sum_{l=i,j,k} \{-\nabla_l \phi(\mathbf{m}) \nabla_l \tilde{u}(\mathbf{m}) + [1-\phi(\mathbf{m})] \nabla_l^2 \tilde{u}(\mathbf{m})\}. \tag{A11}$$

In Eq. (A11), we calculate the spatial derivatives in the i direction using the following second order centered difference formulas:

$$\nabla_i u(i,j,k) = \frac{u(i,j,k)(a_{i+1}^2 - a_{i-1}^2) + u(i+1,j,k)a_{i-1}^2 - u(i-1,j,k)a_{i+1}^2}{a_{i+1}a_{i-1}(a_{i+1}+a_{i-1})}, \tag{A12}$$

$$\nabla_i^2 u(i,j,k) = 2\frac{u(i+1,j,k)a_{i-1} + u(i-1,j,k)a_{i+1} - u(i,j,k)(a_{i-1}+a_{i+1})}{a_{i+1}a_{i-1}(a_{i+1}+a_{i-1})}, \tag{A13}$$

where a_{i-1} and a_{i+1} are the distances between the centers of the elements $\mathbf{m}=(i,j,k)$ and $(i-1,j,k)$ and $(i+1,j,k)$, respectively. The position of the center of the element $\mathbf{r}_{\text{center}}(\mathbf{m})$, is taken at the origin of the coordinate system local to the element $\mathbf{m}$, i.e., at $\xi=0$, $\eta=0$, $\zeta=0$; this yields $\mathbf{r}_{\text{center}}(\mathbf{m})=\frac{1}{8}\Sigma_{n=1}^{8}\mathbf{r}_{\mathbf{n}}(\mathbf{m})$ with the above choice of the shape functions. We derived Eqs. (A12) and (A13) using the approximations of the functions $u(i+1,j,k)$ and $u(i-1,j,k)$ obtained by the expansion of these functions into the second order Taylor polynomials with respect to the corresponding distances between the neighboring elements. The spatial derivatives in the j and k directions are calculated in the same manner. We note that for the case of the nondeformed regular lattice where $a_{i-1}=a_{i+1}=a$, the above expressions reduce to the conventional second order centered difference formulas with equal spacing, i.e., $\nabla_i u(i,j,k)=[u(i+1,j,k)-u(i-1,j,k)]/2a$ and $\nabla_i^2 u(i,j,k)=[u(i+1,j,k)+u(i-1,j,k)-2u(i,j,k)]/a_2$.

[1] *Nonlinear Dynamics in Polymeric Systems*, edited by J. A. Pojman and Q. Tran-Cong-Miyata, ACS Symposia Series No. 869 (ACS, Washington, D.C., 2004).
[2] M. Shibayama and T. Tanaka, Adv. Polym. Sci. **109**, 1 (1993).
[3] A. P. Dhanarajan, G. P. Misra, and R. A. Siegel, J. Phys. Chem. A **106**, 8835 (2002).
[4] T. G. Szanto and G. Rabai, J. Phys. Chem. A **109**, 5398 (2005).
[5] K. Kurin-Csorgei, I. R. Epstein, and M. Orban, Nature (London) **433**, 139 (2005).
[6] A. Ryan *et al.*, Nano Lett. **6**, 73 (2006).
[7] J. Boissonade, Phys. Rev. Lett. **90**, 188302 (2003).
[8] *Reflexive Polymers and Hydrogels: Understanding and Designing Fast Responsive Polymeric Systems*, edited by N. Yui, R. Mrsny, and K. Park (CRC Press, Boca Raton, FL, 2004).
[9] J. Boissonade, Chaos **15**, 023703 (2005).
[10] V. V. Yashin and A. C. Balazs, Macromolecules **39**, 2024 (2006).
[11] V. V. Yashin and A. C. Balazs, Science **314**, 798 (2006).
[12] V. V. Yashin and A. C. Balazs, J. Chem. Phys. **126**, 124707 (2007).
[13] B. P. Belousov, *Collection of Short Papers on Radiation Medicine* (Medgiz, Moscow, 1959); A. N. Zaikin and A. M. Zhabotinsky, Nature (London) **225**, 535 (1970).
[14] T. Yamaguchi, L. Kuhnert, Zs. Nagy-Unvarai, S. C. Muller, and B. Hess, J. Phys. Chem. **95**, 5831 (1991).
[15] R. Yoshida, T. Takahashi, T. Yamaguchi, and H. Ichijo, J. Am. Chem. Soc. **118**, 5134 (1996).
[16] R. Yoshida, E. Kokufuta, and T. Yamaguchi, Chaos **9**, 260 (1999).
[17] R. Yoshida, Curr. Org. Chem. **9**, 1617 (2005).
[18] R. Yoshida *et al.*, J. Phys. Chem. A **104**, 7549 (2000).
[19] T. Sakai and R. Yoshida, Langmuir **20**, 1036 (2004).
[20] R. Yoshida *et al.*, J. Phys. Chem. A **103**, 8573 (1999).
[21] O. Kuksenok, V. V. Yashin, and A. C. Balazs, Soft Matter **3**, 1138 (2007).
[22] V. Labrot, P. De Kepper, J. Boissonade, I. Szalai, and F. Gauffre, J. Phys. Chem. B **109**, 21476 (2005).
[23] D. M. Holloway and L. G. Harrison, Ann. Bot. (London) **101**, 361 (2008).
[24] S. K. Scott, *Oscillations, Waves, and Chaos in Chemical Kinetics* (Oxford University Press, New York, 1994).
[25] J. J. Tyson and P. C. Fife, J. Chem. Phys. **73**, 2224 (1980).
[26] B. Barriere and L. Leibler, J. Polym. Sci., Part B: Polym. Phys. **41**, 166 (2003).
[27] R. J. Atkin and N. Fox, *An Introduction to The Theory Of Elasticity* (Longman, New York, 1980).
[28] S. Hirotsu, J. Chem. Phys. **94**, 3949 (1991).
[29] T. Amemiya, T. Ohmori, and T. Yamaguchi, J. Phys. Chem. A **104**, 336 (2000).
[30] S. Sasaki, S. Koga, R. Yoshida, and T. Yamaguchi, Langmuir **19**, 5595 (2003).
[31] I. M. Smith and D. V. Griffiths, *Programming the Finite Element Method* (Wiley, Chichester, England, 2004).
[32] O. C. Zienkiewicz and R. L. Taylor, *The Finite Element Method* (Butterworth-Heinemann, Oxford, England, 2000),

Vol. 1.

[33] We note that the linear hexahedral element was chosen for the simplicity. Any other element could be chosen, but all of the forces and integrals should be recalculated according to a procedure similar to the one described above. There is, however, no need to choose a more complex element since the model is robust with the above choice.

[34] We note that the actual run time for the simulation results shown in Fig. 3 (from $t=0$ until $t=2000$ with the time steps specified at the end of the model section) took 26 min on a single processor Intel Northwood 3.2 GHz.

[35] In the simulations presented in Fig. 3, as well as in the simulations presented below, we chose the standard deviation to be equal 0.05; we note, however, that any other choice of the standard deviation leads to identical results in terms of regular periodic oscillations at late times. More specifically, we compared the evolution of the same system for the cases when we start with the much smaller or larger initial fluctuation (taking the standard deviations within the range from 0.0001 to 0.9) and confirmed that the late-time oscillations always were identical to the ones shown in Fig. 3.

[36] The vertical lines in Fig. 7 between the data points at $f=f_L^*$ and data points corresponding to regular oscillations (marked with blue, dark blue and green colors online for $L=2$, 6, and 12, respectively) simply serve as a guide for the eye; there are no simulation data points along these vertical lines.

[37] R. Aihara and K. Yoshikawa, J. Phys. Chem. A **105**, 8445 (2001).

[38] S. Maeda, Y. Hara, R. Yoshida, and S. Hashimoto, Adv. Mater. Res. **19**, 3480 (2007).